



Original Article

Start-to-end modeling and transmission efficiency optimization for a cyclotron-based proton therapy beamline

Yu Chen, Bin Qin*, Xu Liu, Wei Wang, Yicheng Liao

State Key Laboratory of Advanced Electromagnetic Technology, School of Electrical and Electronic Engineering, Huazhong University of Science and Technology, Wuhan, 430074, China

ARTICLE INFO

Keywords:

Start-to-end modeling
Monte Carlo simulation
Transmission efficiency optimization
Multi-objective Bayesian optimization

ABSTRACT

Utilizing first-order beam dynamics models is adequate for studying the beam properties during the conceptual design of a cyclotron-based proton therapy beamline. After finishing lattice design, particle-matter interaction simulations for passive elements (e.g., degrader, collimators, energy slit) are required. The cascade simulation is used for lattice updates in each iteration, which is complicated. In addition, when the models involve particle tracking and particle-matter interaction, their optimization process is time-consuming. Therefore, this study proposes a start-to-end modeling method using Monte Carlo Beam Delivery Simulation (BDSIM) software that considers more realistic factors, such as particle-matter interaction and the realistic vacuum chamber, to precisely evaluate working parameters, along with an efficient optimization method that utilizes multi-objective Bayesian optimization (MOBO) to improve transmission efficiency. Taking the Huazhong University of Science and Technology proton therapy facility (HUST-PTF) as an example, beam loss along the beamline is located, quantified, and subsequently reduced by tuning the quadrupole strengths based on MOBO. The results show that: (i) By considering the particle-matter interaction and the realistic vacuum chamber, the precision in the prediction of the beam properties is improved; (ii) After optimization, the transmission efficiency of the entire beamline is relatively increased by an average of 6.52 % under different energy settings, especially 11.39 % at 70 MeV.

1. Introduction

Proton therapy is a radiotherapy treatment that precisely delivers protons with varying energies to diseased tissue to kill cancer cells or shrink target volume [1]. The overall beam transport process in proton therapy involves two crucial processes: beam dynamics and energy modulation. In a cyclotron-based facility, the multiple scattering within a degrader controls the energy degradation. As a side effect of the energy degradation, the beam emittance and momentum spread are increased significantly [2]. To ensure the desired beam quality at the patient's location, known as the isocenter, a series of passive elements (e.g., degrader, collimators, energy slit) are employed to shape the beam.

Currently, several codes are available for simulating beam transport in proton therapy beamlines. However, it is challenging to encompass all the necessary physics processes within a single code. The overall beam transport simulation typically necessitates using two distinct types of codes. Beam dynamics codes, such as TRANSPORT [3] and MAD-X [4], are employed to calculate the optics parameters in beamline

components like quadrupoles, dipoles, and drifts. Monte Carlo codes like TURTLE [5], GEANT4 [6], FLUKA [7], and TOPAS [8] are utilized to evaluate Coulomb scattering and energy loss in the degrader, collimators, and energy slit [9]. In previous works [10–12], first-order optical matching of the beamline was conducted using beam dynamics code TRANSPORT; the multi-wedge energy degrader and the downstream collimators/energy slit were designed and validated using Monte Carlo codes GEANT4 and TURTLE. The code chain TRANSPORT-GEANT4-TURTLE is used for lattice updates in each iteration.

Nonetheless, a drawback arises when employing multiple codes: the output of one code must be converted to a format required by the following code, and some assumptions are made during this conversion process. For example, after simulating the particles passing through the energy degrader and collimators using GEANT4, their kinetic energy distribution is assumed to approximate a Gaussian distribution and inputted into TURTLE. However, it is not a strict Gaussian distribution due to the energy tailing effect. Therefore, still utilizing multiple codes

* Corresponding author.

E-mail address: bin.qin@hust.edu.cn (B. Qin).

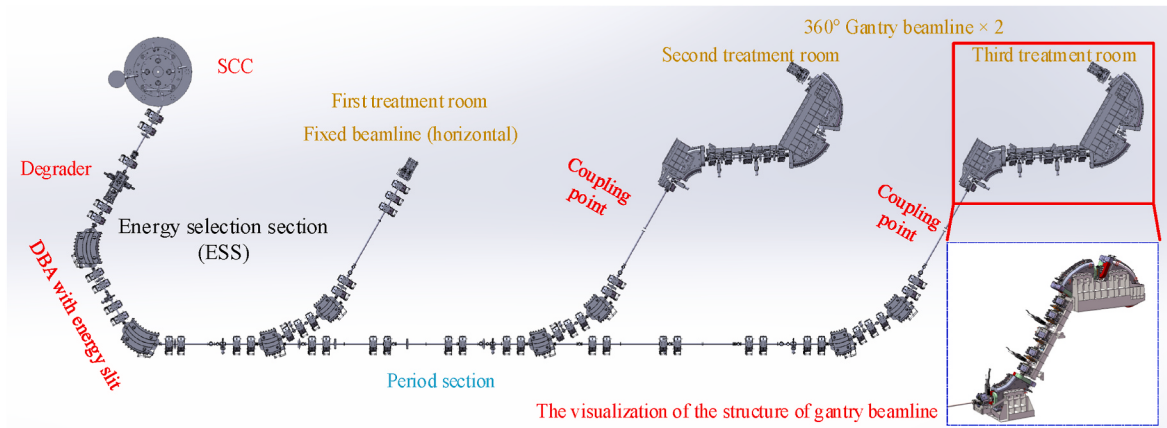


Fig. 1. The overall layout of the HUST-PTF. The beamline of this study goes from the cyclotron to the second treatment room.

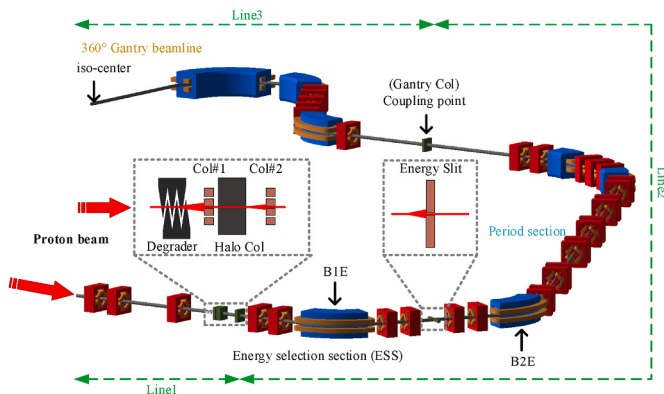


Fig. 2. HUST-PTF beamline modeled by BDSIM.

to study the beam properties after finalizing the lattice design is cumbersome, error-prone, and time-consuming. Thus, there is a desire for a single model that integrates beam dynamics and energy modulation to obtain and evaluate optimal working parameters as the lattice design evolves and during beam commissioning.

Building a more precise start-to-end model for the proton therapy system beamline is not a new topic. Refs. [13–15] used Beam Delivery Simulation (BDSIM) to build beamline models for proton therapy systems and conducted start-to-end simulations to evaluate radiation protection quantities and monitor concrete shielding activation. In addition, the Refs. [16,17] exhibit a high level of agreement between simulation results in BDSIM and experimental measurements in beam properties. Ref. [18] used the Object Oriented Parallel Accelerator Library (OPAL) to build the integrated beam dynamics model for improving precision in predicting the beam properties, which was validated on experimental measurements. Ref. [19] developed a modular Python library Georges for seamless beam dynamics simulations by implementing the Fermi-Eyes technique. From the results of the above references, it is concluded that integrating beam dynamics and energy modulation to achieve start-to-end simulation is more precise than modeling each section separately.

Once the established models involve Monte Carlo simulation and particle tracking, they generally require substantial simulation time. The iterative process of tuning the parameters of beamline components through repeated simulations is time-consuming. Although some

optimization algorithms can make tuning beamline components' parameters more intelligent, they still need much time for repeated simulations. Ref. [20] proposed a surrogate model based on neural networks to accelerate this process, but conducting many simulations to obtain data is still inevitable. Therefore, developing an efficient optimization method for these models is imperative.

Inspired by the works above, this study aims to evaluate the proton therapy beamline accurately and quickly optimize the beamline components' parameters. We construct an integrated model to conduct start-to-end simulations and propose an efficient transmission efficiency optimization method based on the multi-objective Bayesian optimization (MOBO).

The remainder of this study is organized as follows: model setup and methodology are introduced in Section II; results are presented in Section III; and Section IV provides conclusions.

2. Model setup and methodology

2.1. Details and model of HUST-PTF beamline

Huazhong University of Science and Technology is constructing a proton therapy facility (HUST-PTF) based on a 240 MeV superconducting cyclotron accelerator [21,22]. As depicted in Fig. 1, the HUST-PTF consists of a superconducting cyclotron accelerator, a beam transport line, and three treatment rooms (one fixed and two rotating 360°) for clinical treatment. Generally, several sections are required for a cyclotron-based proton therapy facility: (i) An energy selection section (ESS) modulates the beam energy and quality; (ii) A beam switchyard and periodic section delivers the beam to a specific treatment room; (iii) A fixed or gantry beamline delivers the beam to the treatment nozzle. Currently, the lattice and magnet design for the HUST-PTF have been finalized, and all the magnets have been installed on the beamline.

BDSIM, based on Geant4, is an advanced toolkit for Monte Carlo simulation of particle motion [23]. The Monte Carlo simulation of Coulomb scattering and energy loss is performed with particle tracking. Moreover, the influence of passive elements on beam emittance and momentum spread can be analyzed in addition to the linear optics. The version used in this study is BDSIM-v1.6.0. Fig. 2 shows the constructed HUST-PTF beamline model based on BDSIM. In Fig. 2, the extracted beam is focused by a quadrupole triplet onto a degrader consisting of 2 pairs of 3 graphite wedges, enabling the adjustment of proton energies within the range of 230–70 MeV. Behind the degrader, the combination

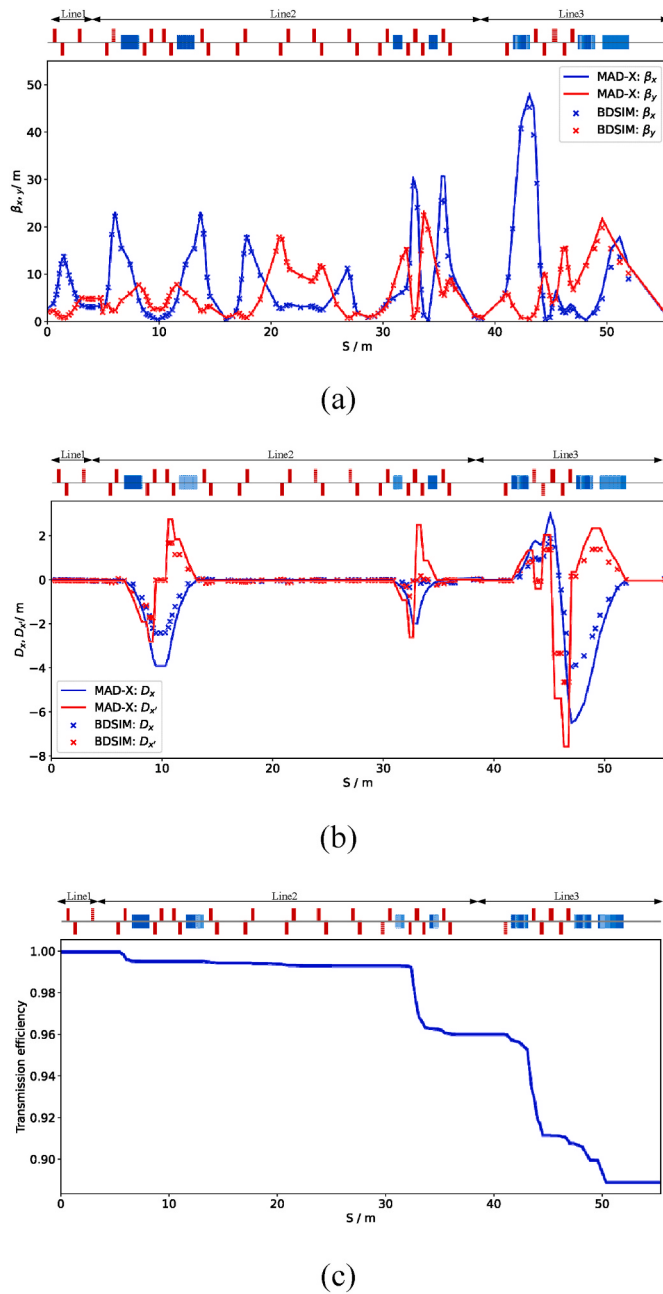


Fig. 3. The comparison results of optical parameters and beam transmission under opening collimators, slit, and degrader. (a). β_x and β_y . (b). D_x and $D_{x'}$. (c). beam transmission.

of three collimators and energy slit in double-bend achromatic (DBA) are used to control beam emittance and momentum spread. Then, the periodic section efficiently delivers the beam with minimal loss to the coupling point through the FODO cell structure. The Gantry collimator ensures that the beam entering the Gantry beamline is round, which is advantageous for achieving a consistent round-shaped beam at the isocenter.

In BDSIM, the sampler plane is placed at the exit of each element, and

data collection and post-processing are done on the sampler plane. To avoid the influence of secondary particles generated by particle-matter interaction on relevant statistical calculations, "stopSecondaries" is set to stop the secondary particle simulation. To speed up relevant calculations, "beamPipesInfiniteAbsorber" is set to remove particles that collide with the material of the vacuum chamber. According to Ref. [24], the physics list "g4QBBC", whose pure hadronic part consists of elastic, inelastic, and capture processes, is chosen. In addition, the modeling process considers vacuum chamber models, including a circular vacuum chamber and two rectangular vacuum chambers.

It is necessary to compare the optical parameters to demonstrate the consistency between the BDSIM-based model and the optical design. Since optical code can't simulate the particle-matter interaction, the HUST-PTF beamline, excluding the passive elements, is divided into three sections (Line1, Line2, Line3) for optical parameter verification according to the collimators' position shown in Fig. 2. Since this process does not involve beam loss caused by energy modulation, 20k particles are used to verify the optical parameters. The optical parameters calculated by BDSIM are compared with the design results obtained from the MAD-X code, as shown in Fig. 3. In Fig. 3c, it's clear that the transmission efficiency falls short of the $\geq 95\%$ design expectation. Therefore, this study will focus on optimizing the transmission efficiency.

2.2. Evaluation of the beam properties

An appropriate method for calculating beam statistical parameters, such as rms emittance ϵ , kinetic energy E_k , momentum spread $\frac{\Delta p}{p}$, etc., is beneficial in evaluating the beam properties. Generally, all particles contribute to calculating beam statistical parameters. However, due to particle-matter interactions, some outlier particles have excessive divergence and cannot be transmitted to the isocenter, as shown in Fig. 4. Some beam statistical parameters will be overestimated because of outlier particles. Therefore, a three-sigma cut is proposed in Ref. [2] to reasonably evaluate beam emittance growth during energy degradation, as shown in Eq. (1). Particles that satisfy the three-sigma cut are collected, with subsequent data post-processing done to derive the beam statistical parameters.

$$\begin{cases} -3\sigma_x \leq x \leq 3\sigma_x \\ -3\sigma_y \leq y \leq 3\sigma_y \\ -3\sigma_{x'} \leq x' \leq 3\sigma_{x'} \\ -3\sigma_{y'} \leq y' \leq 3\sigma_{y'} \end{cases} \quad (1)$$

where σ_x , σ_y , $\sigma_{x'}$, and $\sigma_{y'}$ are the standard deviations obtained by fitting the distributions of x , y , x' , and y' using Gaussian distribution.

This study makes some improvements to the data post-processing proposed in Ref. [2], which are as follows:

- (1). The calculation of statistical kinetic energy and momentum spread: There are generally three methods for calculating the beam statistical kinetic energy and momentum spread: (i) Calculate the E_k and σ_E using the pure statistical method where the mean is the E_k , and the standard deviation is the σ_E ; (ii) The beam kinetic energy distribution is fitted by the Gaussian distribution with the mean as the E_k and the standard deviation as the kinetic energy spread σ_E ; (iii) Obtaining the peak value of the kinetic energy as E_k and using the full-width half maximum (FWHM) of the kinetic energy peak to calculate σ_E ($\sigma_E = \text{FWHM}/2.355$). For all methods, $\frac{\Delta p}{p}$ can be calculated from the σ_E . This

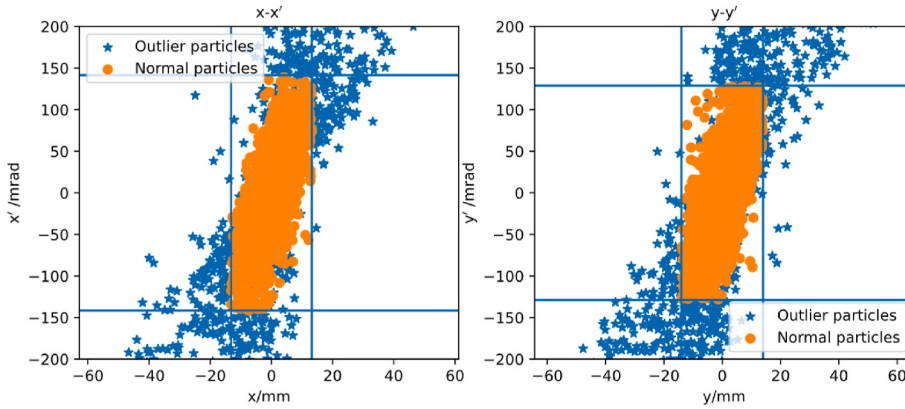


Fig. 4. The example of outlier particles in degrader at 70 MeV. The blue line is the value of $\pm 3\sigma_{x, y, x', y'}$. These outlier particles are caused by collisions during energy modulation. (For interpretation of the references to colour in this figure legend, the reader is referred to the Web version of this article.)

study excludes outlier particles by the three-sigma cut and then uses the (ii) to calculate E_k and $\frac{\Delta p}{p}$. **Fig. 5** shows the beam kinetic energy distribution after Col#2 and B1E at 70 MeV and 230 MeV, including the beam kinetic energy and momentum spread calculated by these three methods. As shown by the constructed Gaussian curves in **Fig. 5**, the curve obtained by the fitting method is closer to the beam kinetic energy distribution than the other two methods because the fitting method can alleviate the interference caused by the energy tailing effect.

- (2). The evaluation of beam properties after the ESS: To mitigate the influence of the energy tailing effect and outlier particles on calculations after energy degradation, the improvement in (1) only aims at beam transport in the ESS. However, after the beams pass through the ESS, there is almost no energy tailing effect and a host of outlier particles, and the transmission efficiency of the subsequent beamline is above 95 %. Therefore, all particles contribute to evaluating the beam properties after the ESS. The normal peripheral particles will be excluded if the three-sigma cut is continually used.

In addition, it should be noted that the transmission efficiency is calculated without using the three-sigma cut, but directly counts the number of particles reaching the sampler plane of each element.

2.3. Basic principle of MOBO

Based on the specific beam loss illustrated in **Fig. 3c**, the intuitive idea is to adjust quadrupole strengths at positions involving high beam loss. Given the imperative of maximizing transmission efficiency, it's also essential for the beam properties to adhere to 1:1 image optics, so employing multi-objective optimization (MOO) is suitable for addressing this problem. Moreover, in cases where calculating objective function (i.e. using the BDSIM-based model to calculate transmission and beam properties) involves high computational costs, MOBO, which is proven to be effective under a small amount of initial observation [25, 26], becomes essential due to its sample efficiency. The observation and evaluation in MOBO represent the input (i.e. quadrupole strengths) and output (i.e. transmission efficiency and beam properties) of the objective function, respectively. MOBO utilizes the Gaussian process (GP) to

establish a posterior probability distribution through the combination of observation and corresponding evaluation at each iteration and then uses the acquisition function to intelligently obtain the next observation most likely to contain the global optimal solution. **Fig. 6** is an illustrative example of the single-objective Bayesian optimization.

This study uses the sparse axis-aligned subspace (SAAS) GP and the parallel noise expected hypervolume improvement (qNEHVI) as the acquisition function for MOBO, which currently is a state-of-the-art combination among high-dimensional problems [27]. The SAAS GP is defined as follows:

$$\begin{aligned} k^{\psi} &= \sigma_k^2 \exp \left\{ -\frac{1}{2} \sum_i \rho_i (x_i - y_i)^2 \right\} \\ [\text{kernel variance}] \quad \sigma_k^2 &\sim LN(0, 10^2) \\ [\text{global shrinkage}] \quad \tau &\sim HC(0.1) \\ [\text{length scales}] \quad \rho_i &\sim HC(\tau) \text{ for } i = 1, \dots, D. \\ [\text{function values}] \quad f &\sim N(0, K^{\psi}) \text{ with } \psi = \{\rho_{td}, \sigma_k^2\} \\ [\text{observation}] \quad f &\sim N(f, 0.001E_{n \times n}) \end{aligned} \quad (2)$$

where k^{ψ} is the RBF kernel, K^{ψ} is the kernel matrix, LN denotes the log-normal distribution, HC denotes the half-Cauchy distribution, N is the Gaussian distribution, D is the input space, E is the identity matrix, and n is the number of observations. The qNEHVI integrates the acquisition function over the posterior $p(\psi|O)$ of the SAAS GP hyperparameters ψ given the observations O and is defined as follows:

$$\alpha_{\text{qNEHVI-MCMC}}(X_{\text{cand}}) = \int_{\psi} \alpha_{\text{qNEHVI}}(X_{\text{cand}}|\psi) p(\psi|O) d\psi \quad (3)$$

where α_{qNEHVI} is the function based on hypervolume improvement (HVI) and X_{cand} denotes new candidates. Considering the complexity of the principles, this study only offers a foundational overview of SAAS GP and qNEHVI. For further insights into the application of SAAS GP and qNEHVI, readers can see Refs. [28,29]. The specific process is shown in Algorithm 1.

Algorithm 1. This study outlines the main steps of transmission efficiency optimization based on MOBO.

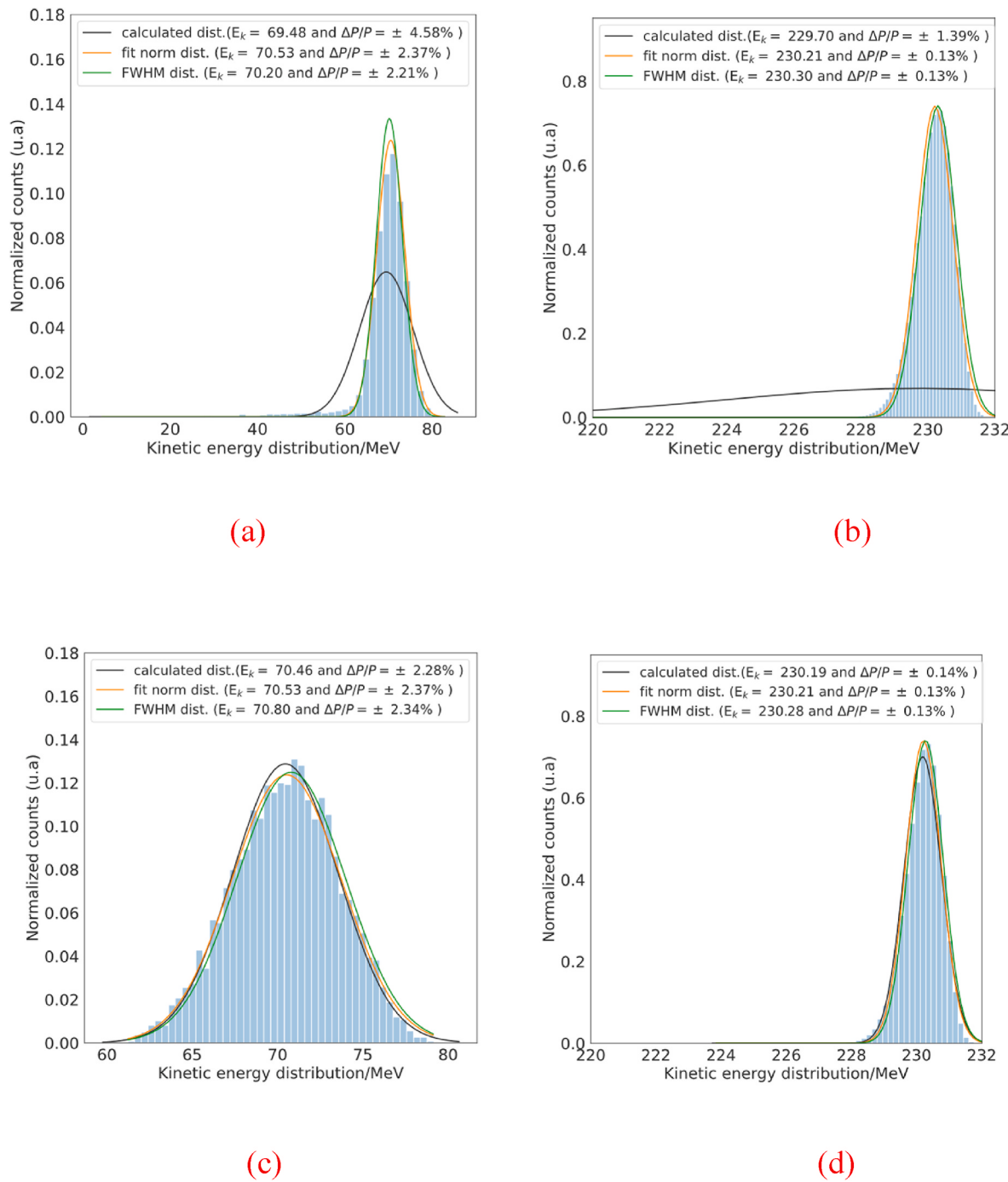


Fig. 5. The beam kinetic energy distribution after using the three-sigma cut to exclude outlier particles. At low energies, the accuracy of calculating the kinetic energy and momentum spread using the purely statistical method drops. Errors occur when calculating beam energy in the low-energy range using FWHM. (a). Col#2: 70 MeV. (b). Col#2: 230 MeV. (c). B1E: 70 MeV. (d). B1E: 230 MeV.

Input: Objective functions $f_{obj} = (f^{(1)}(x), \dots, f^{(7)}(x))$, initial evaluation budget $m \geq 2$, total evaluation budget $T > m$, initial observation set $x_{1:m}$, and evaluations $y_{1:m}$ (optional). // x and y are vector values that contain multiple quadrupole strengths and objectives (Satisfying 1:1 image optics and maximizing transmission efficiency at isocenter), respectively.

Output: Based on evaluations, manually choose the best observation x_{best}, y_{best} in the Pareto-optimal set.

1. Set the original quadrupole strengths within ± 0.5 as the bounded search space $X, x \in X$.
2. If $x_{1:m}, y_{1:m}$ is not provided, let $x_{1:m}$ be a Sobol sequence and let $y_t = f_{obj}(x_t), x_t \in X$, for $t=1, \dots, m$.
// Construct the initial observation set and get evaluations.
3. **for** $t=m+1, \dots, T$ **do**
4. Let $H_t = \{x_{1:t-1}, y_{1:t-1}\}$.
5. Use H_t to fit SAAS GP.
6. Use QNEHVI to obtain the next observation x_t .
7. Evaluate $y_t = f_{obj}(x_t)$. // Input the observation into the BDSIM-based model to obtain an evaluation
8. **end**

Return Pareto-optimal set $\{x_{1:a}, y_{1:a}\}$.

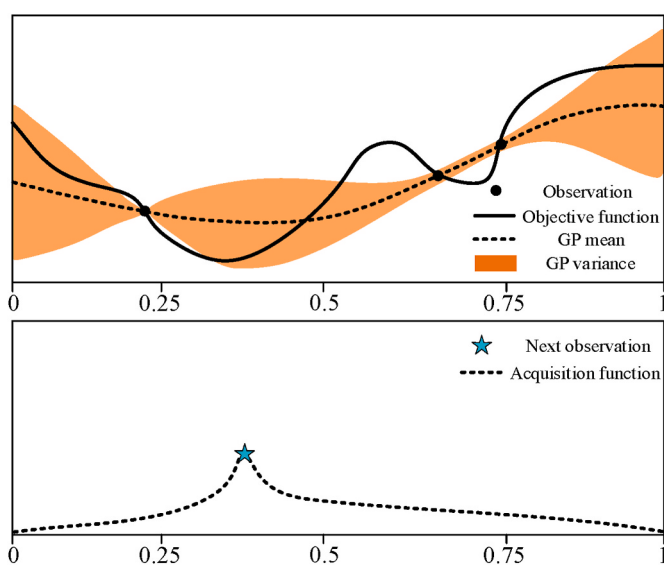


Fig. 6. Example of single-objective BO. A black-box surrogate model, such as the GP, is established based on existing observations. This surrogate model, in combination with an acquisition function, guides decision-making on the probable location of the minimum point for objective function while considering uncertainty. The next observation in this figure is determined by the surrogate model trained by the initial three observations and the acquisition function.

3. Results

This section provides the application of MOBO to obtain a new set of quadrupole strengths. Subsequently, the obtained quadrupole strengths are used to conduct start-to-end simulations.

3.1. Beam properties optimization of the beamline design from Col#2 to isocenter

Fig. 3c shows that the transmission efficiency of Line1 is nearly 100 %, while Line2 and Line3 exhibit transmission efficiencies of 95.8 % and 92.44 %, respectively. From **Fig. 3a**, it can be seen that there are some discrepancies between the optical parameters calculated by BDSIM and MAD-X in Line2 and the gantry beamline (i.e., Line3). In particular, noticeable beam loss occurs at the third dipole in Line2 and the first dipole in the gantry beamline. The primary reason for beam loss stems from the fact that the geometric shape of the vacuum chambers is not considered in the optical design. In Line2, the vacuum chambers of dipole (rectangle, 90 mm \times 71 mm) and quadrupole (circular, radius

Table 1
Bounded search space and optimization objectives.

Optimization object	Bounded search space	Objectives
Line2	The last seven quadrupoles (original quadrupole strengths within ± 0.5)	Minimize $ \sigma_x - 2.5 , \sigma_y - 2.5 , \sigma_x - 2.8 , \sigma_y - 2.8 , D_x , D_x' $ and maximize transmission efficiency
Gantry beamline	All six quadrupoles (original quadrupole strengths within ± 0.5)	Minimize $ \sigma_x - 2.5 , \sigma_y - 2.5 , \sigma_x - 2.8 , \sigma_y - 2.8 , D_x , D_x' $ and maximize transmission efficiency

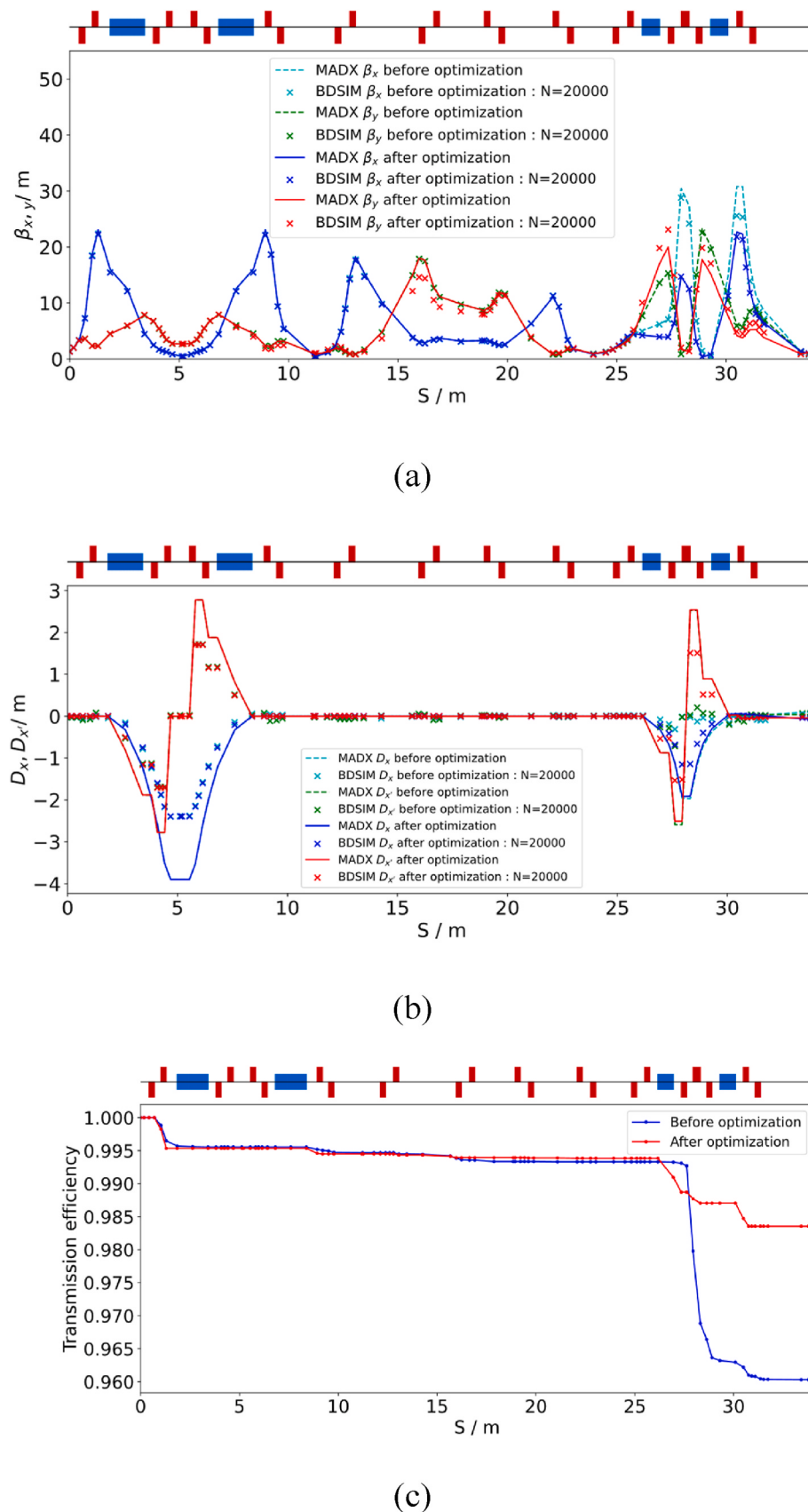


Fig. 7. The comparison results of optical parameters and beam transmission in Line2 before and after optimization. (a). β_x and β_y . (b). D_x and $D_{x'}$. (c). beam transmission.

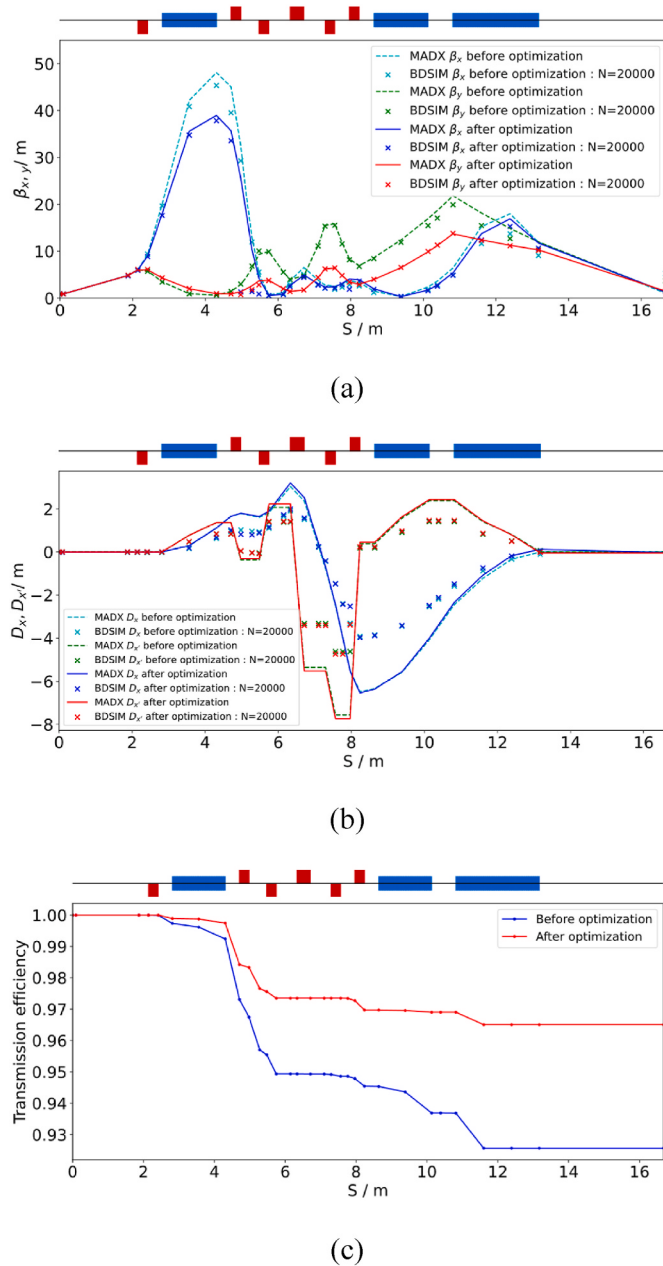


Fig. 8. The comparison results of optical parameters and beam transmission in Line3 before and after optimization. (a). β_x and β_y . (b). D_x and D_x' . (c). beam transmission.

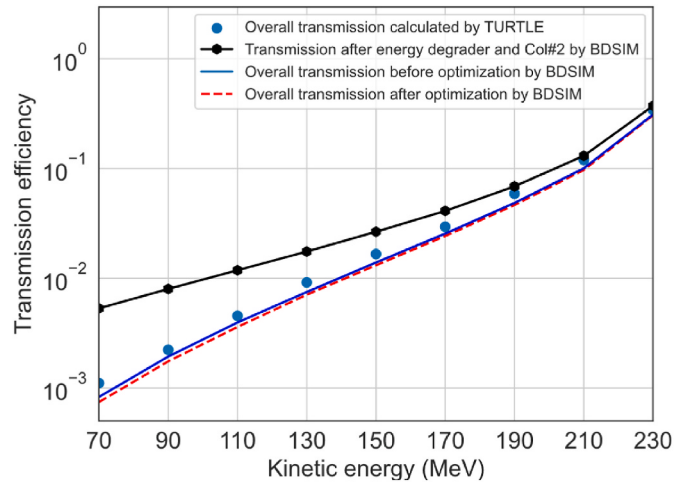


Fig. 9. The comparison of transmission efficiency. "Overall transmission calculated by Turtle" represents calculating transmission efficiency by TURTLE without consideration of the energy tailing effect. "Overall transmission after (before) optimization" represents the transmission of the original (optimal, i.e. obtained quadrupole strengths in Section III.1) design.

36.55 mm) mismatch, resulting in beam truncation during beam transport. In the gantry beamline, the beam envelope in the x-direction becomes too large after entering the first dipole, leading to collisions of peripheral particles with the vacuum chamber, which explains why the β_x in BDSIM is smaller than that obtained from the MAD-X code.

Based on the above analysis, a new set of quadrupole strengths, encompassing the last seven quadrupoles of Line2 and all six quadrupoles of the gantry beamline, can be separately tuned by MOBO to satisfy the 1:1 image optics and maximize transmission efficiency. Table 1 lists the bounded search spaces and optimization objectives. Figs. 7 and 8 show the optical parameters, dispersion, and beam transmission after optimization, with Line2 and the gantry beamline exhibiting 98.36 % and 96.41 % transmission efficiencies, respectively. Figs. 7 and 8 show the optics parameters calculated by BDSIM closely align with those derived from the MAD-X code, indicating the mitigation of collision after optimization. This conclusion can also be drawn from the beam loss in Figs. 7c and 8c.

In addition, it should be noted that improved beam properties compared to the initial optics design are achieved for both Line2 and the gantry beamline, demonstrating a certain level of generalizability of the proposed method. Moreover, many current beamline designs utilize 1:1 image optics [10,16,17] and the proposed optimization scheme also follows suit, which can provide some reference value for other related works.

Table 2

The beam properties at the exit of the typical elements under 70 MeV and 230 MeV. This study only applies the three-sigma cut in the ESS.

Energy setting	With the three-sigma cut				Without the three-sigma cut			Transmission Efficiency (%)
	Element	$\epsilon_x(\text{pi-mm-mard})$	$\epsilon_y(\text{pi-mm-mard})$	$\frac{\Delta P}{P} (\% 1\sigma)$	$\epsilon_x(\text{pi-mm-mard})$	$\epsilon_y(\text{pi-mm-mard})$	$\frac{\Delta P}{P} (\% 1\sigma)$	
70 MeV	Deg	137.22	148.21	2.40	470.38	490.81	5.3	67.46
	Col#2	7.41	7.45	2.37	40.77	38.45	8.02	5.31
	Energy slit	29.43	6.84	0.38	127.83	43.78	4.19	0.09
	Coupling point	6.97	7.08	0.38	6.82	7.08	0.31	0.08
	isocenter	7.62	7.21	0.38	6.69	7.20	0.31	0.08
230 MeV	Deg	10.95	13.35	0.12	24.74	29.28	0.16	97.09
	Col#2	5.15	5.49	0.13	113.47	113.27	13.68	37.25
	Energy slit	11.43	5.12	0.13	12.59	6.80	0.55	31.17
	Coupling point	4.74	5.13	0.13	4.77	5.14	0.13	31.15
	isocenter	4.82	5.14	0.13	4.76	5.14	0.13	31.12

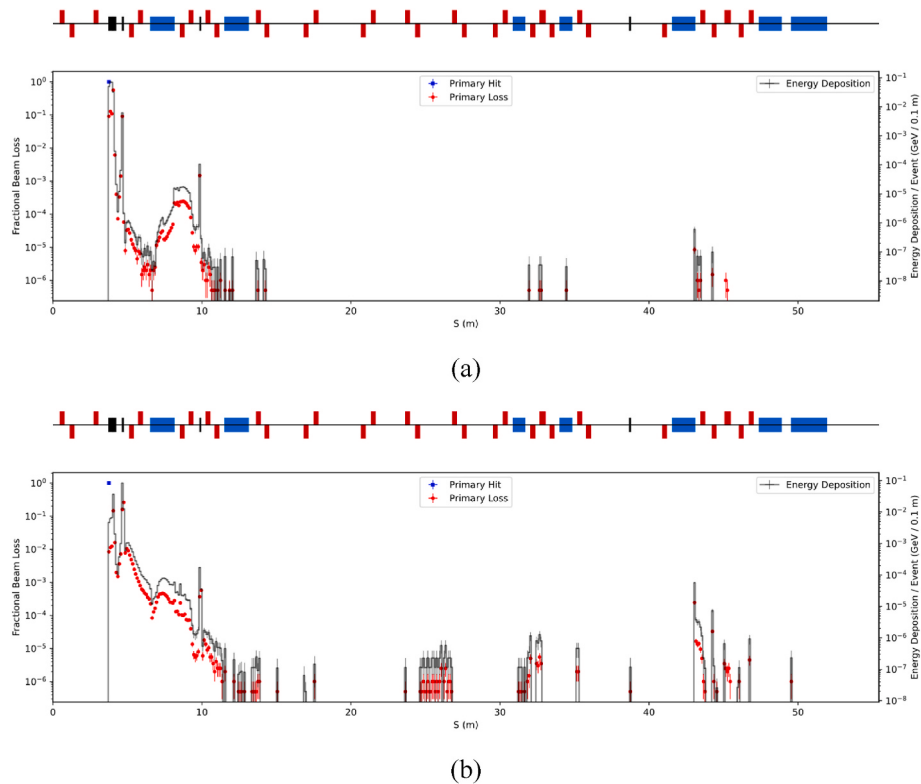


Fig. 10. The beam loss and energy deposition during the beam transport. The "Primary Hit" represents the fraction of the primary beam that undergoes its first interaction. The "Primary Loss" represents the fractional beam losses per unit length. The "Energy Deposition" represents the energy deposited by the primaries. All the particles interact with the degrader, resulting in the absence of downstream primary hits. (a). 70 MeV. (b). 230 MeV.

3.2. Start-to-end simulation of the HUST-PTF beamline design from entrance to isocenter

The obtained quadrupole strengths are used to conduct start-to-end simulations integrating beam dynamics and energy degradation for studying the beam properties with 2000k initial particles. Previous work [11] has calculated the thickness of the graphite wedge at each energy setting and the distance of the energy slit at each momentum spread (using constant distance at $\frac{\Delta p}{p} = 0.3\% \sigma$). Table 2 shows the beam properties at 70 MeV and 230 MeV energy settings. The results from Table 2 indicate that (i) Evaluating beam properties in the ESS without applying the three-sigma cut is overestimated due to the presence of outlier particles. (ii) Supposing the three-sigma cut continues to be used after the particles pass through the ESS, normal peripheral particles will be removed, leading to some beam properties being overestimated.

Fig. 9 presents the comparison of transmission efficiency under various energy settings. Compared to the original design under different energy settings, an average relative improvement of 6.52 % in transmission efficiency is obtained, especially 11.39 % at 70 MeV. On the other hand, the results calculated by BDSIM align with those calculated by TURTLE on the high-energy range's transmission efficiency. However, a significant deviation in the low-energy range is becoming more pronounced as energy decreases. The reasons are: (i) TURTLE assumes that the beam distribution after degrader is Gaussian distribution without considering the energy tailing effect. (ii) The influence of the geometric shape of the vacuum chamber is not considered.

To further verify the correctness of the above analysis, Fig. 10 shows the beam loss and energy deposition during the beam transmission. From Figs. 5 and 10, it can be seen that (i) The lower the energy setting, the more severe the energy tailing effect. (ii) Due to the energy tailing effect, many particles deviate from the central energy, colliding with the vacuum chamber of the B1E. So, the energy tailing effect is reduced after the B1E. (iii) At 230 MeV, the proportion of particles that deviate from

the central energy after Col#2 is smaller than that at 70 MeV, so the energy tailing effect is not as severe as at 70 MeV. The lower the energy setting, the greater the difference between the transmission efficiency calculated by BDSIM and TURTLE.

Furthermore, this study calculates the transmission efficiency under the constraint ($\frac{\Delta p}{p} < 0.6 \% 2\sigma$). The Col#2 transmission efficiency (0.09 %), meets the constraint at 70 MeV, already lower than that (0.11 %) calculated by TURTLE. In addition, this value is close to transmission efficiency at 70 MeV (0.08 %), so the downstream beamline actually delivers particles whose momentum spread satisfies this constraint.

It should be noted that the proposed modeling method contributes to a more precise and convenient evaluation of the existing beamline design. Furthermore, the calculated transmission efficiency provides valuable insights for devising the beam intensity modulation scheme for subsequent treatments.

4. Conclusions

This study proposes start-to-end modeling and transmission efficiency optimization methods for a cyclotron-based proton therapy beamline based on BDSIM and MOBO. Based on the above results, the following conclusions are drawn:

- (1) The BDSIM-based model can guide transmission efficiency optimization by locating and quantifying the beam loss. While studying the beam properties, the energy tailing effect after energy degradation should be considered, which becomes more severe as the energy decreases and is mitigated when the beam passes through the subsequent dipole.
- (2) To accurately evaluate a proton therapy beamline, employing a single model integrating beam dynamics and energy degradation is essential. In addition, applying the three-sigma cut and

adopting appropriate data post-processing methods in the corresponding beamline section is crucial.

Aimlessly adjusting magnet currents on-site for an extended period in future beam commissioning is impractical. The model that exhibits a high degree of consistency with the actual beamline can serve as a surrogate model for beam commissioning. Incorporating all actual magnet field maps into the current constructed model can reduce the difference with the actual beamline, thereby facilitating the exploration of fringe fields and high-order aberrations. In addition, the results of this study indicate the significant impact of the energy tailing effect on transmission efficiency, suggesting that finding a suitable wedge material to mitigate this effect will be a simple and effective method to improve transmission efficiency.

Subsequently, the proposed configuration and calculated transmission efficiency can be validated by measurement data. While BDSIM-based results can be regarded as golden truths, this study is a pure simulation. The extent to which this ultimately corresponds to measurements in the real system remains to be demonstrated in the future.

CRediT authorship contribution statement

Yu Chen: Methodology, Resources, Software, Writing – original draft, Writing – review & editing. **Bin Qin:** Conceptualization, Funding acquisition, Supervision, Writing – original draft, Writing – review & editing. **Xu Liu:** Methodology, Supervision, Writing – review & editing. **Wei Wang:** Writing – review & editing. **Yicheng Liao:** Writing – review & editing.

Declaration of competing interest

The authors declare that they have no known competing financial interests or personal relationships that could have appeared to influence the work reported in this paper.

Acknowledgments

We are very grateful to BDSIM author Laurie Nevay at Royal Holloway, University of London, for providing relevant help when we encountered problems with using BDSIM. This work was supported by the National Natural Science Foundation of China under Grant 11975107 and National Key Research and Development Program of China (No. 2016YFC0105305).

References

- [1] R.R. Wilson, Radiological use of fast protons, *Radiology* 47 (5) (1946) 487–491.
- [2] V. Rizzoglio, A. Adelmann, C. Baumgarten, D. Meer, J. Snuverink, V. Talanov, On the accuracy of Monte Carlo based beam dynamics models for the degrader in proton therapy facilities, *Nucl. Instrum. Methods Phys. Res. Sect. A Accel. Spectrom. Detect. Assoc. Equip.* 898 (2018) 1–10.
- [3] U. Rohrer, "PSI Graphic Transport Framework."
- [4] <http://mad.web.cern.ch/mad/>.
- [5] U. Rohrer, "PSI Graphic Turtle Framework."
- [6] S. Agostinelli, et al., Geant4—a simulation toolkit, *Nucl. Instrum. Methods Phys. Res. Sect. A Accel. Spectrom. Detect. Assoc. Equip.* 506 (3) (2003) 250–303.
- [7] P. R. S. A. Ferrari, A. Fassó, and J. Ranft, "CERN Yellow Report No. CERN-2005-10."
- [8] <http://www.topasmc.org/>.
- [9] M.K. Hamad, Bragg-curve simulation of carbon-ion beams for particle-therapy applications: a study with the GEANT4 toolkit, *Nucl. Eng. Technol.* 53 (8) (2021) 2767–2773.
- [10] B. Qin, et al., Design of gantry beamline for HUST proton therapy facility, *IEEE Trans. Appl. Supercond.* 28 (3) (2018) 1–5.
- [11] Z. Liang, et al., Design and optimization of an energy degrader with a multi-wedge scheme based on Geant4, *Nucl. Instrum. Methods Phys. Res. Sect. A Accel. Spectrom. Detect. Assoc. Equip.* 890 (2018) 112–118.
- [12] W. Chen, et al., Transmission calculation and intensity suppression for a proton therapy system, *Nucl. Instrum. Methods Phys. Res. Sect. A Accel. Spectrom. Detect. Assoc. Equip.* 881 (2018) 82–87.
- [13] C. Hernalsteens, et al., A novel approach to seamless simulations of compact hadron therapy systems for self-consistent evaluation of dosimetric and radiation protection quantities, *Europhys. Lett.* 132 (5) (2020) 50004.
- [14] E. Ramoiaux, C. Hernalsteens, R. Tesse, E. Gnacadja, N. Pauly, F. Stichelbaut, Hybrid monitoring and measurement of concrete shielding activation at the ProtherWal proton therapy centre, *EPJ Tech. Instrum.* 10 (1) (2023) 9.
- [15] E. Ramoiaux, et al., Self-consistent numerical evaluation of concrete shielding activation for proton therapy systems, *Europhys. J. Plus* 137 (8) (2022) 889.
- [16] V. Maradia, D. Meer, D.C. Weber, A.J. Lomax, J.M. Schippers, S. Psoroulas, A new emittance selection system to maximize beam transmission for low-energy beams in cyclotron-based proton therapy facilities with gantry, *Med. Phys.* 48 (12) (2021) 7613–7622.
- [17] V. Maradia, et al., Increase of the transmission and emittance acceptance through a cyclotron-based proton therapy gantry, *Med. Phys.* 49 (4) (2022) 2183–2192.
- [18] V. Rizzoglio, et al., Evolution of a beam dynamics model for the transport line in a proton therapy facility, *Phys. Rev. Accelerat. Beams* 20 (12) (2017) 124702.
- [19] R. Tesse, C. Hernalsteens, E. Gnacadja, N. Pauly, E. Ramoiaux, M. Vanwelde, Georges: a modular Python library for seamless beam dynamics simulations and optimization, *SoftwareX* 24 (2023) 101579.
- [20] A. Edelen, N. Neveu, M. Frey, Y. Huber, C. Mayes, A. Adelmann, Machine learning for orders of magnitude speedup in multiobjective optimization of particle accelerator systems, *Phys. Rev. Accelerat. Beams* 23 (4) (2020) 044601.
- [21] B. Qin, et al., Design and development of the beamline for a proton therapy system, *Nucl. Sci. Tech.* 32 (12) (2021) 138.
- [22] P. Li, et al., Design of HUST-PTF beamline control system for fast energy changing, *Nucl. Eng. Technol.* 54 (8) (2022) 2852–2858.
- [23] L.J. Nevay, et al., BDSIM: an accelerator tracking code with particle-matter interactions, *Comput. Phys. Commun.* 252 (2018) 107200.
- [24] A.V. Ivantchenko, V.N. Ivanchenko, J.-M.Q. Molina, S.L. Incerti, Geant4 hadronic physics for space radiation environment, *Int. J. Radiat. Biol.* 88 (1–2) (2012) 171–175.
- [25] V. Nguyen, Bayesian optimization for accelerating hyper-parameter tuning, in: 2019 IEEE Second International Conference on Artificial Intelligence and Knowledge Engineering (AIKE), 2019, pp. 302–305.
- [26] D. Eriksson, et al., Latency-Aware Neural Architecture Search with Multi-Objective Bayesian Optimization, *abs/2106.211890*.
- [27] https://ax.dev/tutorials/saasbo_nehvi.html.
- [28] D. Eriksson, M. Jankowiak, High-dimensional Bayesian optimization with sparse axis-aligned subspaces, in: Presented at the Proceedings of the Thirty-Seventh Conference on Uncertainty in Artificial Intelligence, Proceedings of Machine Learning Research, 2021.
- [29] S. Daulton, M. Balandat, E. Bakshy, Parallel bayesian optimization of multiple noisy objectives with expected hypervolume improvement, in: Neural Information Processing Systems, 2021.